Energy & Environmental Science

Accepted Manuscript

ROYAL SOCIETY OF CHEMISTRY

www.rsc.org/ees

Energy & Environmental Science RSCPublishing

ARTICLE

A Highly Active Nanostructured Metallic Oxide Cathode for Aprotic Li-O_2 Batteries

Cite this: DOI: 10.1039/x0xx00000x

Dipan Kundu, Robert Black, Erik Jämstorp Berg and Linda F. Nazar*

Received 13th August 2014
Accepted xxx

DOI: 10.1039/x0xx00000x

www.rsc.org/

The aprotic lithium-oxygen cell is based on the reversible reduction of oxygen on a cathode host to form lithium peroxide, and has received much attention in the last few years owing to its promise to offer increased electrochemical energy density beyond that provided by traditional Li-ion batteries. Carbon has been extensively utilized as a host, but it reacts with Li_2O_2 to form an insulating layer of lithium carbonate resulting in high overpotentials on charge. Establishing a stable, and conductive interface at the porous cathode is a major challenge that has motivated a search for non-carbonaceous cathode materials. Very few suitable materials have been discovered so far. Here we report on the synthesis of the metallic Magnéli phase Ti_4O_7 with a crystallite size between 10-20 nm, and show that a cathode fabricated from this material greatly reduces the overpotential compared to carbon. Oxidation of lithium peroxide on charge starts just above 3 V, comparable to gold and TiC, and the majority (~65%) of oxygen release occurs in the 3-3.5 V window vs Li^+/Li as determined by on-line electrochemical mass spectrometry. Ti_4O_7 is much lighter and lower cost than gold, easy to prepare, and provides a controlled interface. X-ray photoelectron spectroscopy measurements show that a conductive, self-passivating substoichiometric metal oxide layer is formed at the surface which is important for stability.

Introduction

The aprotic lithium-oxygen cell (referred to as the Li-air battery) has been the subject of much focus recently. This owes to its promise to offer increased electrochemical energy density per mass beyond that provided by traditional Li-ion batteries.[1,2] Defined by the chemistry of the reversible reaction Li + O_2 ↔ Li_2O_2, the redox couple results in very high specific energy due to the low atomic mass of both reactants and a favorable 3.0 V potential.[3] The theoretical gravimetric energy density of 3,505 Wh/kg (based on Li_2O_2) is very attractive relative to contemporary Li-ion cells that have comparable values near 400 Wh/kg, and speaks to the allure of electrified automotive transport with extended-range driving.[4] Gravimetric energy density will increasingly motivate battery development as future automotive designs allow for more sophisticated accomodation of the battery volume. Practical values for Li-air batteries are estimated near 1000 Wh/kg, but realizing this requires surmounting many challenges in the underlying chemistry.[2,3,4,5]

One of the most prominent of these challenges is developing a chemically stable porous cathode capable of efficient oxygen reduction (ORR) and evolution (OER).[6, 7] Carbon has been extensively utilized for this role, but recent studies show that a lithium carbonate layer forms upon reaction at the interface with superoxide/peroxide.[8, 9] This insulating layer impedes electron flow, creating an electrochemical overpotential for oxygen evolution, driving up the voltage and contributing further to electrolyte decomposition on charge.[9, 10] It is now recognized that establishing a stable, and conductive interface at the porous cathode is of prime importance, motivating the search for non-carbonaceous cathode materials capable of efficient ORR. Few materials have been discovered so far. Amongst these, nanoporous gold is one of the most promising owing to the inert nature of the noble metal and its good ORR activity.[11] It is clearly not suitable for practical applications, however. Cathodes based on oxides such as semiconducting Co_3O_4 and V_2O_5; [12-14] and Al_2O_3-passivated carbon have been employed to good effect,[15] but these materials still present a significant impedance to electron transfer. Most recently, nanocrystalline TiC has been demonstrated by Thiotyl *et al* to be an efficient gas diffusion cathode.[16] It presents the qualities of metallic conductivity in common with gold. Furthermore, formation of a passivating "TiO_2 rich" surface layer on TiC was reported to be vital to the system's cyclability by preventing unwanted side reactions with the electrolyte or reduced oxygen species. Metallic oxides might be expected to be even more advantageous, as they offer the potential to combine excellent underlying bulk electron transport needed for an efficient cathode with a seamless oxide interface. The latter provides necessary catalytic activity for oxygen reduction and passivates the bulk against further reactivity while still facilitating electron transfer.

Amongst potential target conductive oxides, a series of titanium based materials (Ti_nO_{2n-1}), popularly known as Magnéli phases, are particularly promising candidates. They are much less costly and lower weight than nanostructured metallic ruthenium pyrochlores, for example, which have been shown to demonstrate good activity in a Li-O_2 cell.[17, 18] Magnéli titanates have been considered as a potential conductive support in many electrochemical systems.[19-22] This owes to their high conductivity and chemical stability even under highly aggressive conditions.[21-24] They combine the high conductivity of metals[25] and the corrosion resistance of ceramics.[22] Also, as the Magnéli oxide materials are only mildly reduced *vis a vis* the parent oxide, they are expected to be resistant to nucleophilic attack by O_2^-/O_2^{2-} anions and to be promising candidates for good anodic stability in the OER potential

window of interest. In this homologous series of oxide phases, Ti_4O_7 has the highest electrical conductivity (~10^3 S cm^{-1}) at room temperature.[25, 26] Creating an ultra-high surface area modification of this ceramic is a considerable challenge, however. It is generally synthesized from TiO_2 under controlled reducing conditions at high temperatures using hydrogen, carbon, and metals.[27] High processing temperatures not only lead to a lack of control in phase purity but result in dense low surface area materials. The materials are therefore unsuitable as cathodes in a Li-O_2 cell, where high surface area, a large number of active sites for ORR and a porous structure are crucial for performance.[18, 28]

With this in mind, we have developed a facile approach that yields essentially carbon-free, high surface area, porous nanocrystalline Ti_4O_7 at lower temperatures than established reduction methods. We note that its carbon-containing analogue prepared under dissimilar conditions and with different precursors exhibits excellent properties as a cathode for Li-S batteries, as recently reported.[29] The multiporous nano-Ti_4O_7 described here demonstrates reversible oxygen reduction-evolution when employed as a gas diffusion cathode material in Li-O_2 cells, and a very low charge potential onset of 3.0 V vs. Li^+/Li. The majority (~65%) of oxygen release occurs in the 3.0-3.5 V window, which is comparable to oxygen evolution from an Au surface[11] in a non-aqueous Li-O_2 cell in the absence of a redox mediator.

Physical Characterization

The titanium oxide Magnéli phases are a homologous series of triclinic phases of composition Ti_nO_{2n-1} ($4 \leq n \leq 10$) that have structures characterized by two dimensional shear plane slabs of TiO_6 octahedra. Electrical conductivity of these phases is known to vary with *n*. With standard methods of preparation it is very difficult to obtain nanocrystalline pure phases. Our synthetic approach, which utilizes crosslinking of titanium ethoxide with an ethyleneimine oligomer followed by carbothermal reduction (see Methods section for details), leads us to the desired crystalline phase with a high degree of control. The Rietveld analysis of the powder X-ray diffraction (XRD) pattern of the as synthesized Ti_4O_7 (**Figure 1a)** confirms crystallization of the triclinic single phase Ti_4O_7 (see **Table S1**, SI). Moreover, the breadth of the diffraction peaks demonstrates the nanocrystalline nature of the material. The thermodynamic formation energies of different Magnéli titanium oxides (Ti_nO_{2n-1}) are very close under carbothermal reduction conditions in an Ar atmosphere. Precise control of the inorganic to organic precursor ratio in the gel and its decomposition temperature plays a crucial role in the synthesis of phase-pure Ti_4O_7. The material is obtained through this method at a temperature of 860-870°C, which is low compared to that in excess of 1000°C required for the reduction of TiO_2 and which results in significant crystallite growth. Bright field transmission electron microscopy (TEM) investigation reveals the existence of primary particles in the range of 50-100 nm (**Figure 1b)**. A second set of agglomerated fine nanocrystallites can also be seen in the TEM image (marked by arrows). The high resolution transmission electron microscopy image (HRTEM, **Figure 1c**) reveals the existence of Ti_4O_7 crystallites ranging from 10 -20 nm in size, with lattice planes indexed to (110) and (112) based on their d-spacing, further confirming the crystallinity of the phase. Thus, this route is highly effective for confining the particle size to nano dimensions, with a high degree of crystalline order.

Formation of a highly porous structure with high specific surface area was confirmed from N_2 physisorption analysis (**Figure 1d**) that displays a type IV nitrogen adsorption-desorption isotherm (inset). The average pore size of ~2 to 10 nm confirms the micro- and mesoporous texture of the sample. These pores are formed by the decomposition of the organic polymer and the condensation of the inorganic precursor in the precursor gel framework. The accompanying release of gaseous products triggered by the exothermic carbothermal reaction opens up new mesopores and enlarges existing micropores. As a result, the material displays a specific surface area of ~180 m^2 gm^{-1} and a large pore volume of 0.3 cm^3 gm^{-1}. Such high surface area is key for obtaining high oxygen reduction capacities and good rate capability.

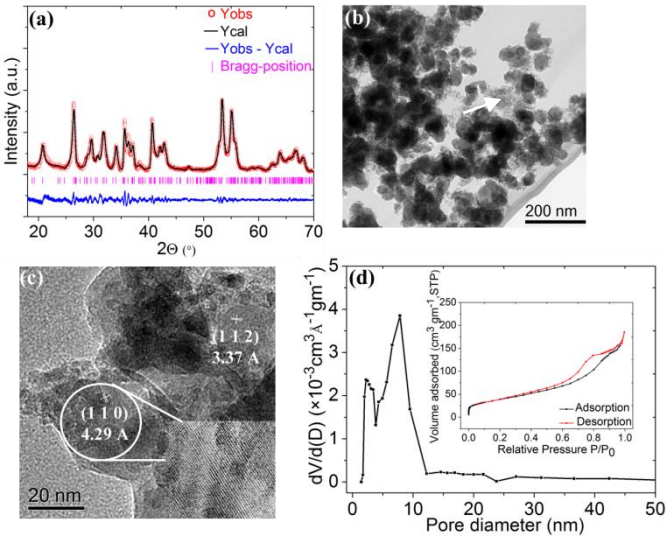

Figure 1. Physical characterization of the Ti_4O_7 nanomaterial. (a) Rietveld refinement of the powder x-ray diffraction pattern of the as synthesized Ti_4O_7. Data points (red circles); calculated profile (black line); difference profile (blue line); Bragg positions (magenta lines). (b) a typical bright field TEM image demonstrating morphology and particle size distribution. The arrows point to the agglomerated fine crystallites. (c) a high resolution TEM image of the Ti_4O_7 nanocrystallites with indexed lattice planes. The (110) lattice planes are expanded in the inset image. (d) pore size distribution of the Ti_4O_7 nanomaterial with the inset image showing the type-IV nitrogen adsorption-desorption BET isotherm.

The room temperature electrical conductivity of this porous Ti_4O_7 is 5 Ω^{-1} cm^{-1}, which is naturally lower than the high values observed for highly crystalline microcrystalline Ti_4O_7, but quite sufficient for electrical transport within the material and to/from the active reaction surface sites. The amount of residual carbon is < 2% as revealed by elemental microanalysis. This very low carbon fraction is not expected to contribute to reactivity with peroxide/superoxide at any significant level.

Electrochemical Studies

Electrochemical cells were constructed as described in the Methods section. The galvanostatic discharge and charge profiles recorded at current densities of 200 uA cm^{-2} and 50 uA cm^{-2} (based on geometric electrode area), respectively, in a potential window of 2.4 V - 4.25 V *vs* Li^+/Li are presented in **Figure 2a**. These confirm the bifunctional capability of the nano-Ti_4O_7 for both ORR and OER. The discharge reaction (ORR) is at an average voltage of 2.65 V, delivering a capacity of 1.2 mAh, equivalent to ~350 mAh g_{Ti4O7}^{-1}. As expected, discharge capacities correlate to the current rate. Galvanostatic discharge at a lower current density of 100 uA cm^{-2} (**Figure S1**, SI) results in a higher specific capacity of ~2.1 mAh/~600 mAhg_{Ti4O7}^{-1}, and demonstrates the very good ORR activity of the Ti_4O_7 nanomaterial. The lower current rate also brings the discharge potential up to 2.7 V. The influence of large specific surface area and the presence of mesopores - which enhances catalyst utility due to higher electrode/electrolyte contact area and improved electrode kinetics - benefit the discharge capacity.

Reduced voltage polarization and consequently improved round trip energy efficiency is achieved.

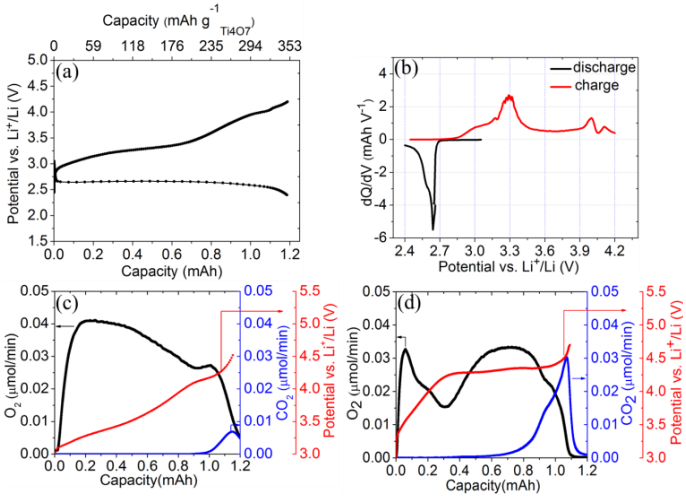

Figure 2. Electrochemistry and OEMS of the Ti_4O_7 cathode in a Li-O_2 cell. (a) galvanostatic discharge and charge profile of a Li-O_2 cell employing Ti_4O_7 nanomaterial as cathode in a potential window of 2.4 V - 4.25 V *vs* Li^+/Li. Discharge and charge current densities were 200 and 50 μA/cm^2, respectively; (b) differential capacity plot obtained from Figure 2a. The peaks in this profile correspond to plateaus in the galvanostatic profile and denote major electrochemical processes during discharge and charge reactions; online mass spectrometry (OEMS) for cells employing (c) Ti_4O_7, and (d) Vulcan carbon cathodes during electrochemical charge of cells pre-discharged to a capacity of 1 mAh. The red, black and the blue curves depict voltage variation, O_2 evolution, and CO_2 evolution, respectively, during galvanostatic charge.

Charging (OER) initiates at a very low voltage of 3 V, very close to the reversible thermodynamic formation/decomposition voltage of 2.96 V. [30, 31] The profile displays a gently rising plateau between 3 and 3.5 V, followed by a sloping region up to ~4 V. Significantly, OER achieves 65% and 85% completion by 3.5 V and 4.0 V, respectively (as confirmed by on-line mass spectrometry, **Figure 2c**; see next section). This indicates the absence of significant cathode corrosion that would lead to higher overpotential on charge. We note that the electrolyte/Ti_4O_7 is stable up to 4.6V (**Figure S2**). The corresponding dQ/dV plot (**Figure 2b**) more clearly illustrates the findings. The narrow peak at 2.65 V represents the ORR process, whereas the broad positive peak centered at around 3.3 V signifies OER; the higher voltage features correspond to electrolyte by-product oxidation (see next section).

The formation and removal of Li_2O_2 upon discharge and charge were visualized by SEM (**Figure S3**). Apparent are the filling of the cathode pores by a film-like product upon discharge at 200 uA cm^{-2} and its removal upon charge. We note that particles of toroidal morphology are formed at a lower current density of 25 uA cm^{-2}, where their lateral dimensions become thinner as the current density increases to 100 uA cm^{-2} (**Figure 3**). Overall, ~10 nm thin discs/platelets are formed at 150 uA cm^{-2} with a transition to a film-like deposition product at 200 uA cm^{-2}. This is consistent with our earlier observation of the current density dependent morphological transition of discharge product formed on an active carbon cathode in a Li-O_2 cell[31]. Moreover, when current densities are normalized with respect to the real surface area obtained from BET analysis, the morphology transition regime for Ti_4O_7 is close to carbon (**Table S2**). The role of the discharge current density on the charging characteristics was singled out by discharging the Li-O_2 cells employing the Ti_4O_7 cathode at different current densities followed by charging at a same current (**Figure S1**). The voltage polarization in overall charge profile decreases when the discharge current density is increased. Again, as in the case of carbon,[31] this is correlated to the chargeability of discharge products with different morphologies. A film like peroxide deposition at a higher current rate leads to a substantially lower overpotential on charging and the complete removal of discharge products. Better round trip energy efficiency results. We note this may well be linked to the formation of amorphous peroxide at high current rates - which is reported to be more ionically conductive than the crystalline phase by a factor of 10^{12} on the basis of calculations[32, 33] - and/or formation of a superoxide-rich surface which lowers the charge potential.[34]

Electrochemical cyclability of the Ti_4O_7 cathode in a Li-O_2 cell was studied by limiting the capacity to 1 mAh. This enabled complete charge below 4 V against Li^+/Li (**Figure S4a**, SI). Good performance is achieved, with a major portion of charge taking place at low potential. The incremental irreversibility introduced into the charging process following the 1st cycle is due to accumulation of glyme and LiTFSI decomposition products that are not fully removed due to the low charge voltage cutoff (see below). Limiting the deliverable capacity to 0.1 mAh and performing the galvanostatic cycling at a high current density of 500 uA cm^{-2} resulted in stable behavior over extended cycling (**Figure S4b**, SI).

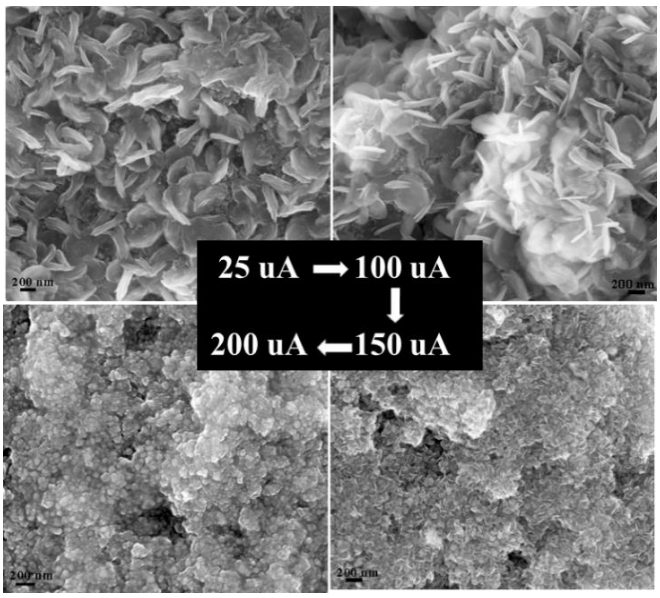

Figure 3. Transition of Li_2O_2 morphology, with variation in discharge current density for the Ti_4O_7 cathode as indicated.

Online Mass Spectrometry (OEMS)

To further explore the effectiveness of Ti_4O_7 as a cathode, mass spectrometry was used to evaluate the gases generated during charge. Mass spectrometry is an invaluable tool for analyzing Li-O_2 OER processes which has been used to study the viability of different electrolytes for the Li-O_2 cell,[9] and to validate the efficiency of different Li-O_2 battery cathodes and possible side products during cell operation.[16, 35] We compared the evolution of gaseous oxygen (m/z = 32) and carbon dioxide (m/z = 44) during cell charge of a Ti_4O_7 electrode to that of Vulcan® carbon XC72 (VC). VC was chosen for comparison as it has a similar surface area to our synthesized Ti_4O_7. Using 0.5 M LiTFSI/TEGDME and a total cell discharge of 1 mAh (see Methods), a charging current density of 250 μA cm^{-2} was applied until oxygen evolution ceased. The results are shown in **Figure 2c** and **Figure 2d**. For Ti_4O_7, the major oxygen evolution occurs well below 3.5 V (**Figure 2c**), in agreement with the lower OER potential for the galvanostatic cycling discussed previously. The Ti_4O_7 cathode exhibits a high rate of oxygen evolution between 3.0 - 3.5 V, which finally diminishes at higher potentials/capacity and ceases at ~ 4.20V. The increase around 4.0V (0.85 mAh) in the curve is due to the

oxidation of residual Li_2O_2, which is inhibited at lower potential by the build-up of electrolyte decomposition products (see below). These must be removed before Li_2O_2 oxidation can be completed, at a capacity of 1.0 mAh that corresponds to the discharge load. In contrast, the VC carbon cathode displays a different oxygen evolution profile (**Figure 2d**): the charging voltage increases sharply and is accompanied by a rapid decay in oxygen evolution between 3.8 and 4 V, followed by further oxygen evolution at ~4.4 V.

By combining OER with the charge current, we can calculate the $(e^-/O_2)_{chg}$ for both cells, which is a measure of the Coulombic efficiency. The value should be 2.0 if the only process on charge is the oxidation of lithium peroxide. However, as is well known, almost all studies show $(e-/O_2)_{chg}$ >>2.0,[36] which implies that some parasitic electrochemistry always occurs during the charging process. The TEGDME/Ti_4O_7 cell exhibits an $(e^-/O_2)_{chg}$ of 2.6 whereas for VC, the $(e^-/O_2)_{chg}$ values were higher. These varied between 2.8 and 3.4 e-/O_2 depending on current rate. Similar values have been observed for VC with glyme electrolytes in previous reports.[8, 37] The higher value for VC is the result of interfacial oxidation of carbon by reactive oxygen,[9, 10] leading to the formation of an additional insulating interlayer of Li_2CO_3 between Li_2O_2 and the active carbon surface. This impedes the Li_2O_2 oxidation until a higher charging potential is reached, which strips the Li_2CO_3. The accompanying evolution of significant CO_2 in the high voltage charging region is characteristic of the decomposition of Li_2CO_3. Contrary to VC, much less CO_2 is evolved in the case of Ti_4O_7. Here, it must be associated with the oxidation of glyme decomposition products such as lithium formate and acetate.[38] While electrolyte decomposition is an issue that must be resolved if the Li-O_2 battery is to achieve its full potential, it is not within the scope of this manuscript. The comparison of gas evolution clearly shows that the Ti_4O_7 lowers the oxidization overpotential of the Li_2O_2 compared to carbon by about 0.3 - 0.5 V over the entire charge process. The suppression of carbonate formation at the peroxide/host interface lowers the overpotential thus reducing electrolyte decomposition. Although this is not completely eliminated, the Ti_4O_7 also does not aggravate electrolyte decomposition as do some highly catalytically active transition metal oxides such as RuO_2.[39, 40]

Efficiency of the Ti_4O_7 for OER is further demonstrated by the galvanostatic charging of the Ti_4O_7 cathode preloaded with bulk commercial Li_2O_2 (of crystallize size between 200 - 450 nm, determined by SEM). Charging of Li_2O_2 is achieved at a flat voltage of 3.8 V vs $Li^{+/}Li$ (**Figure 4**). The potential is higher than the initial close-to-equilibrium potential of 3 – 3.3V for the full cell owing to the much larger crystallite size of the commercial peroxide, and much poorer contact with the Ti_4O_7 host. As the charge approaches the quantitative oxidation of peroxide based on the loaded mass (2.0 mAh), the voltage rises, signifying the end of the process. At this point, a trace of CO_2 is evolved, most likely from residual Li_2CO_3 present in the commercial peroxide (see Methods). We also cannot rule out reaction of the electrolyte with evolved superoxide that would also result in carbonate-type products. In any case, the CO_2/O_2 ratio in the evolved gas is overwhelmingly less than in **Figure 2c**. What is clear is that electrochemical oxygen evolution from crystalline peroxide is different from the peroxide formed electrochemically, as we have shown in greater detail in a separate publication.[41] The difference here is also illustrated by the fact that the e^-/O_{2chg} ratio is 2.42 for the prefilled electrode (similar to our prefilled TiC cathode that yields e^-/O_{2chg} =2.45 under identical conditions[39]), which is notably less than measured above for charging the electrochemically formed Li_2O_2 on Ti_4O_7 ($(e^-/O_2)_{chg}$ = 2.60). This is due to the less complex nature of the crystalline peroxide surface and the lower fraction of electrolyte decomposition products (i.e., side reactions). As has been recognized elsewhere for other cathode materials, for the true effectiveness of the Ti_4O_7 on ORR and OER to be realized, an electrolyte that is stable to the Li-O_2 chemistry must be used. DMSO is a very promising candidate, as shown by Mohammed et. al.[16] However, other reports suggest that this may not be the case,[36, 42] indicating that it reacts with Li_2O_2 on prolonged contact to form LiOH[43]. In our hands, DMSO was actually less effective than TEGDME, and did not enable full charge of the cell up to the voltage where it decomposes (4 V).

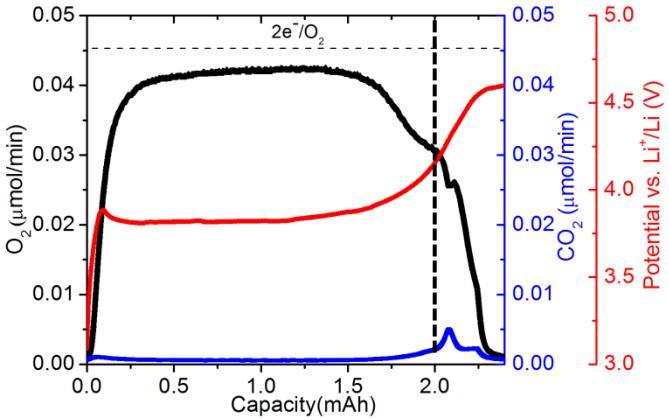

Figure 4. OEMS data for electrochemical charging of a cathode containing nano-Ti_4O_7 preloaded with commercial Li_2O_2 in a weight ratio of Ti_4O_7:Li_2O_2:PTFE :: 8:1:2. The cell was galvanostatically charged at 75 uA cm^{-2}. The red, black and the blue curves depict voltage variation, O_2 evolution, and CO_2 evolution, respectively.

Ex-situ XPS studies on the Ti_4O_7 cathodes

XRD studies on cycled electrodes showed the Magnéli phase was retained (unchanged) upon cycling, without the appearance of any additional new peaks. Efforts to study peroxide formation and decomposition upon electrochemical discharge and charge were unsuccessful, however, due to the superposition of the broad peaks of the Ti_4O_7 nanomaterial on that of the Li_2O_2. In this regard, X-ray photoelectron spectroscopy (XPS) proved to be an effective tool to probe the formation-removal of the peroxide on the cathode and detect any possible corrosion of the Ti_4O_7 surface. **Figure 5a** compares the Li1s XPS spectra of the pristine, discharged and charged cathode. The Li1s region for the discharged cathode includes contribution from the underlying Li_2O_2 (Li1s: 54.5 eV)[14, 44] and surface lithium carbonate species (Li1s: 55.3 eV)[14, 44] formed by the decomposition of glyme electrolyte in contact with lithium peroxide. The intensities of the peaks are not representative of the actual fractions of material present, owing to the extreme surface sensitivity of XPS (~5 nm probe depth). Upon charging, the Li1s peaks corresponding to lithium peroxide disappear to further reveal the surface carbonate species. The surface carbonate peak likely also includes contributions from RCOOLi, and ROLi type products that are formed at the active surface.

Figure 5b shows the Ti_{2p} XPS spectrum of the pristine Ti_4O_7 cathode, where the signal is fit with Ti_4O_7 ($2p_{3/2}$: 459.5 eV), and a slightly more oxygen-rich Magnéli phase which resides on the surface (Ti_5O_9, $2p_{3/2}$: 459.3 eV), both identical to that reported in the literature.[45] Both components were necessary for a good fit. The Ti_5O_9 naturally forms as a native oxide layer on Ti_4O_7 under ambient conditions. As XPS probes only the first 3 -7 nm of any surface, and Ti_4O_7 is still visible in the spectrum, this layer must be extremely thin. The high binding energies of the conductive Magnéli phases are characteristic of their itinerant electron delocalization. A trace of TiO_2 is also present ($2p_{3/2}$: 458.6 eV)[46] on the surface.

The Ti_4O_7 and Ti_5O_9 peaks of the pristine material disappear after the 1st discharge and consecutive charge (**Figure 5b**, upper), indicating partial oxidation of only the Ti_4O_7 surface in contact with Li_2O_2.[24] XRD data of the cycled cathode showed only the presence of Ti_4O_7 (**Figure S5**), indicating its bulk chemical stability. This is not surprising, as this Magnéli phase is known to be stable to corrosion.[21-24]

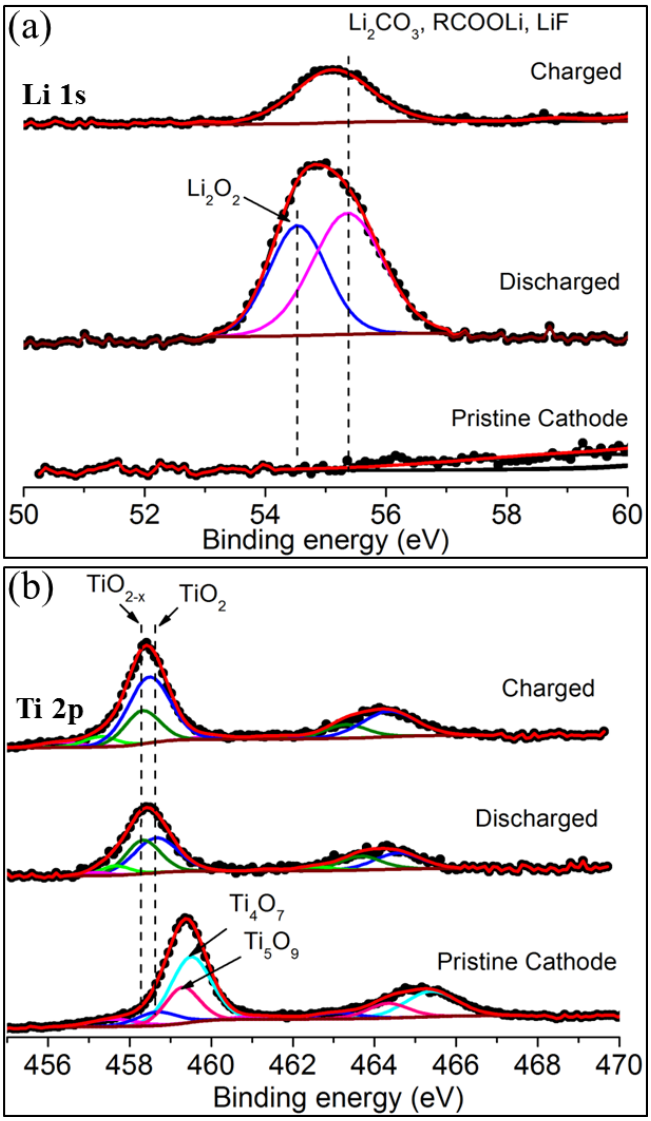

Figure 5. (a) Li 1s, and (b) Ti 2p XPS spectra of the Ti_4O_7 cathode at the pristine, 1st discharged and 1st charged state, respectively, galvanostatically cycled in a 0.5 M LiTFSI-TEGDME electrolyte at 200 uA cm^{-2} for discharge, and 200 uA cm^{-2} discharge followed by 50 uA cm^{-2} charge for the charged cathode.

Two components were necessary for an adequate fit: surface TiO_2, and substoichiometric TiO_{2-x}, based on the lowering of the XPS binding energy ($2p_{3/2}$: 458.3 eV) by 0.3 eV compared to TiO_2. Values for TiO_{2-x} in the literature vary widely, depending on x.[40,47] In our case, x can be estimated based on the fact that reduction from Ti^{4+} to Ti^{3+} results in an overall linear negative shift in binding energy of about 1.5 eV.[47,48] A difference of 0.3 eV thus corresponds to an average oxidation state of $Ti^{3.8+}$. This energy difference is similar to that between Ti_4O_7 ($Ti^{3.5+}$) and Ti_4O_9 ($Ti^{3.6+}$). Importantly, TiO_{2-x} substoichiometric oxides are electronically conductive,[21, 49] albeit less than the underlying metallic Magneli phases. As demonstrated by the effective oxidation of Li_2O_2 from the Ti_4O_7 surface, this TiO_{2-x} interphase facilitates electron flow from the electrochemical reaction sites. A scheme which illustrates this concept is shown in **Figure 6**.

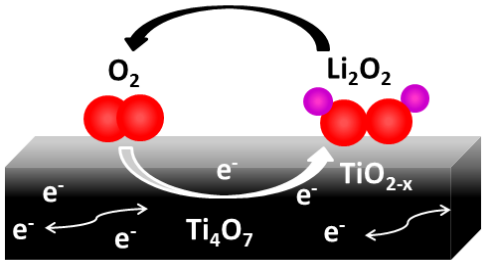

Figure 6. Scheme showing the gradual gradient of sub-stoichiometric TiO_{2-x} formed at the surface of the conductive Magnéli Ti_4O_7 cathode host in the Li-O_2 cell that acts as a thin passivating interphase.

Conclusions

Amongst the most significant challenges facing rechargeable aprotic Li-O_2 batteries are achieving effective oxygen reduction, a low charging potential on oxygen evolution and a stable lithium peroxide-cathode interface. A critical step towards accomplishing those goals is to tackle the issue of cathode corrosion by the Li-O_2 cell discharge product (Li_2O_2) and/or the reactive oxygen species generated during cell charging. In this work, using electrochemical measurements, OEMS, SEM, and XPS, we have shown that a new nanostructured Ti_4O_7 Magnéli phase functions as an effective bifunctional ORR-OER support by reducing the charging voltage and thereby enhancing the round trip energy efficiency. Along with the intrinsic chemical stability of Ti_4O_7, substantial improvement in the voltage polarization can be attributed to its tailored properties which are crucial to ORR. These properties include high specific surface area and porosity that enable facile diffusion to the active sites, and the metallic conductivity of Ti_4O_7 that enables electron transfer from the reaction sites. It is proposed that the stability of the conductive TiO_{2-x} interface is also responsible for the reversible Li_2O_2 formation/oxidation, where the majority of oxygen release (~65%) occurs in the 3-3.5 V window vs Li^+/Li. This is comparable to oxygen evolution from a gold surface in the absence of a redox mediator. Significantly, these results demonstrate the fabrication of a practical cathode for a rechargeable aprotic Li-O_2 battery. Nevertheless, this study also shows that development of novel cathode materials for Li-O_2 batteries cannot be treated separately from the issues related to the electrolyte. For the real assessment of any material's ORR/OER properties, it is essential to have a stable electrolyte system and the opposite also holds true.

Acknowledgements

We thank NRCan for financial support through their EcoEII program, and NSERC through funding from their Discovery Grant and Chair programs. D.K acknowledges partial support of research as part of the Joint Center for Energy Storage Research, an Energy Innovation Hub funded by the U.S. Department of Energy, Office of Science, Basic Energy Sciences. R.B thanks NSERC for a graduate fellowship.

Supplementary information

Electronic Supplementary Information (ESI) available: detailed experimental methods, electrochemical data, XPS and additional FESEM images are provided. This material is available free of charge via the Internet. See DOI: 10.1039/b000000x/

Notes and references

1. J.-S. Lee, S. Tai Kim, R. Cao, N.-S. Choi, M. Liu, K. T. Lee and J. Cho, *Adv. Energy Mater.*, 2011, **1**, 34-50.
2. P. G. Bruce, S. A. Freunberger, L. J. Hardwick and J.-M. Tarascon, *Nat. Mater*, 2012, **11**, 19-29.
3. Y.-C. Lu and Y. Shao-Horn, *J. Phys. Chem. Lett.*, 2012, **4**, 93-99.
4. K. G. Gallagher, S. Goebel, T. Greszler, M. Mathias, W. Oelerich, D. Eroglu and V. Srinivasan, *Energy Environ. Sci.*, 2014, **7**, 1555-1563.
5. R. Black, B. Adams and L. F. Nazar, *Adv. Energy Mater.*, 2012, **2**, 801-815.
6. L. J. Hardwick and P. G. Bruce, *Curr. Opin. Solid State Mater. Sci.*, 2012, **16**, 178-185.
7. F. Li, T. Zhang and H. Zhou, *Energy Environ. Sci.*, 2013, **6**, 1125-1141.
8. B. D. McCloskey, D. S. Bethune, R. M. Shelby, T. Mori, R. Scheffler, A. Speidel, M. Sherwood and A. C. Luntz, *J. Phys. Chem. Lett.*, 2012, **3**, 3043-3047.
9. B. D. McCloskey, A. Speidel, R. Scheffler, D. C. Miller, V. Viswanathan, J. S. Hummelshøj, J. K. Nørskov and A. C. Luntz, *J. Phys. Chem. Lett.*, 2012, **3**, 997-1001.
10. M. M. Ottakam Thotiyl, S. A. Freunberger, Z. Peng and P. G. Bruce, *J. Am. Chem. Soc.*, 2012, **135**, 494-500.
11. Z. Peng, S. A. Freunberger, Y. Chen and P. G. Bruce, *Science*, 2012, **337**, 563-566.
12. Y. Cui, Z. Wen and Y. Liu, *Energy Environ. Sci.*, 2011, **4**, 4727-4734.
13. H. Lee, Y.-J. Kim, D. J. Lee, J. Song, Y. M. Lee, H.-T. Kim and J.-K. Park, *J. Mater. Chem. A*, 2014, **2**, 11891-11898.
14. Y.-C. Lu, E. J. Crumlin, G. M. Veith, J. R. Harding, E. Mutoro, L. Baggetto, N. J. Dudney, Z. Liu and Y. Shao-Horn, *Sci. Rep.*, 2012, **2**.
15. J. Lu, Y. Lei, K. C. Lau, X. Luo, P. Du, J. Wen, R. S. Assary, U. Das, D. J. Miller, J. W. Elam, H. M. Albishri, D. A. El-Hady, Y.-K. Sun, L. A. Curtiss and K. Amine, *Nat. Commun.*, 2013, **4**.
16. M. M. Ottakam Thotiyl, S. A. Freunberger, Z. Peng, Y. Chen, Z. Liu and P. G. Bruce, *Nat. Mater*, 2013, **12**, 1050-1056.
17. S. H. Oh and L. F. Nazar, *Adv. Energy Mater.*, 2012, **2**, 903-910.
18. S. H. Oh, R. Black, E. Pomerantseva, J.-H. Lee and L. F. Nazar, *Nat. Chem*, 2012, **4**, 1004-1010.
19. P. Paunović, O. Popovski, E. Fidančevska, B. Ranguelov, D. Stoevska Gogovska, A. T. Dimitrov and S. Hadži Jordanov, *Int. J. Hydrogen Energy*, 2010, **35**, 10073-10080.
20. F. C. Walsh and R. G. A. Wills, *Electrochim. Acta*, 2010, **55**, 6342-6351.
21. J. R. Smith, F. C. Walsh and R. L. Clarke, *J. Appl. Electrochem.*, 1998, **28**, 1021-1033.
22. P. Krishnan, S. G. Advani and A. K. Prasad, *J. Solid State Electrochem.*, 2012, **16**, 2515-2521.
23. X. Y. Zhang, Y. Liu, J. W. Ye and R. J. Zhu, *Micro Nano Lett.*, 2013, **8**, 251-253.
24. X. Li, A. L. Zhu, W. Qu, H. Wang, R. Hui, L. Zhang and J. Zhang, *Electrochim. Acta*, 2010, **55**, 5891-5898.
25. R. F. Bartholomew and D. R. Frankl, *Phys. Rev.*, 1969, **187**, 828-833.
26. M. Weissmann and R. Weht, *Phys. Rev. B*, 2011, **84**.
27. C. Tang, D. B. Zhou and Q. Zhang, *Mater. Lett.*, 2012, **79**, 42-44.
28. S. Ma, L. Sun, L. Cong, X. Gao, C. Yao, X. Guo, L. Tai, P. Mei, Y. Zeng, H. Xie and R. Wang, *J. Phys. Chem. C*, 2013, **117**, 25890-25897.
29. Q. Pang, D. Kundu, M. Cuisinier, L.F. Nazar, *Nat. Commun.*, 2014.
30. Y.-C. Lu, H. A. Gasteiger, M. C. Parent, V. Chiloyan and Y. Shao-Horn, *Electrochem. Solid-State Lett.*, 2010, **13**, A69-A72.
31. B. D. Adams, C. Radtke, R. Black, M. L. Trudeau, K. Zaghib and L. F. Nazar, *Energy Environ. Sci.*, 2013, **6**, 1772-1778.
32. F. Tian, M. D. Radin and D. J. Siegel, *Chem. Mater.*, 2014, **26**, 2952-2959.
33. K. C. Lau, R. S. Assary, P. Redfern, J. Greeley and L. A. Curtiss, *J. Phys. Chem. C*, 2012, **116**, 23890-23896.
34. J. Yang, D. Zhai, H.-H. Wang, K. C. Lau, J. A. Schlueter, P. Du, D. J. Myers, Y.-K. Sun, L. A. Curtiss and K. Amine, *Phys. Chem. Chem. Phys.*, 2013, **15**, 3764-3771.
35. S. Meini, N. Tsiouvaras, K. U. Schwenke, M. Piana, H. Beyer, L. Lange and H. A. Gasteiger, *Phys. Chem. Chem. Phys.*, 2013, **15**, 11478-11493.
36. A. C. Luntz and B. D. McCloskey, *Chem. Rev.*, 2014, **114**, 11721-11750.
37. B. D. McCloskey, D. S. Bethune, R. M. Shelby, G. Girishkumar and A. C. Luntz, *J. Phys. Chem. Lett.*, 2011, **2**, 1161-1166.
38. B. D. McCloskey, A. Valery, A. C. Luntz, S. R. Gowda, G. M. Wallraff, J. M. Garcia, T. Mori and L. E. Krupp, *J. Phys. Chem. Lett.*, 2013, **4**, 2989-2993.
39. B. D. Adams, R. Black, C. Radtke, Z. Williams, B. L. Mehdi, N. D. Browning and L.F. Nazar., *ACS Nano*, 2014.
40. H.-C. Kim, *Progress in Battery 500 Project. IBM Research-Almaden Research Center, ILABS 2014 International Li-Air Battery Symposium*, Seoul, Korea.
41. S. Ganapathy, B. D. Adams, G. Stenou, M. S. Anastasaki, K. Goubitz, X.-F. Miao, L. F. Nazar and M. Wagemaker, *J. Am. Chem. Soc.*, 2014, **136**, 15807-15808.
42. D. S. Doron Aurbach , Michal Afri, A. A. and F. a. A. Garsuch, *224th ECS Meeting*, 2013, **Abstract #276**.
43. D. G. Kwabi, T. P. Batcho, C. V. Amanchukwu, N. Ortiz-Vitoriano, P. Hammond, C. V. Thompson and Y. Shao-Horn, *J. Phys. Chem. Lett.*, 2014, 2850-2856.
44. R. Younesi, S. Urbonaite, K. Edström and M. Hahlin, *The J. Phys. Chem. C*, 2012, **116**, 20673-20680.
45. C. H. Yao, F. Li, X. Li and D. G. Xia, *J. Mater. Chem.*, 2012, **22**, 16560-16565.
46. C. Rüdiger, F. Maglia, S. Leonardi, M. Sachsenhauser, I. D. Sharp, O. Paschos and J. Kunze, *Electrochim. Acta*, 2012, **71**, 1-9.
47. G. Luca Artiglia, *PhD Dissertation*, University of Padova, 2011.
48. A. F. Carley, P. R. Chalker, J. C. Riviere and M. W. Roberts, *J. Chem. Soc., Faraday Trans. 1: Phys. Chem. Cond. Phases*, 1987, **83**, 351-370.
49. A. M. Zaky and B. P. Chaplin, *Environ. Sci. Technol.*, 2013, **47**, 6554-6563.